Pore-scale modeling of two-phase flow: A comparison of the generalized network model to direct numerical simulation

Luke M. Giudici ©,* Ali Q. Raeini ©, Takashi Akai ©, Martin J. Blunt ©, and Branko Bijeljic ©

Department of Earth Science and Engineering, Imperial College London, London SW7 2AZ, United Kingdom

Despite recent advances in pore-scale modeling of two-phase flow through porous media, the relative strengths and limitations of various modeling approaches have been largely unexplored. In this work, two-phase flow simulations from the generalized network model (GNM) [Phys. Rev. E **96**, 013312 (2017); Phys. Rev. E **97**, 023308 (2018)] are compared with a recently developed lattice-Boltzmann model (LBM) [Adv. Water Resour. **116**, 56 (2018); J. Colloid Interface Sci. **576**, 486 (2020)] for drainage and waterflooding in two samples—a synthetic beadpack and a micro-CT imaged Bentheimer sandstone—under water-wet, mixed-wet, and oil-wet conditions. Macroscopic capillary pressure analysis reveals good agreement between the two models, and with experiments, at intermediate saturations but shows large discrepancy at the end-points. At a resolution of 10 grid blocks per average throat, the LBM is unable to capture the effect of layer flow which manifests as abnormally large initial water and residual oil saturations. Critically, pore-by-pore analysis shows that the absence of layer flow limits displacement to invasion-percolation in mixed-wet systems. The GNM is able to capture the effect of layers, and exhibits predictions closer to experimental observations in water and mixed-wet Bentheimer sandstones. Overall, a workflow for the comparison of pore-network models with direct numerical simulation of multiphase flow is presented. The GNM is shown to be an attractive option for cost and time-effective predictions of two-phase flow, and the importance of small-scale flow features in the accurate representation of pore-scale physics is highlighted.

I. INTRODUCTION

A thorough understanding of multiphase flow through permeable media is essential to a variety of important applications such as oil recovery [1], groundwater flow [2], carbon capture and storage [3], polymer electrolyte membranes [4], and surgical masks [5]. Specifically, the ability to accurately predict multiphase behavior at the micron scale, or pore-scale, is vital to a successful and optimized implementation of such applications. To achieve predictive capability at the pore-scale, many numerical modeling approaches have been developed. These approaches can be divided into two broad categories: direct numerical simulations (DNS)—high fidelity models solving the governing flow equations through detailed geometry; and pore-network models (PNM)—lower fidelity approximations which preserve only the essential geometry. In recent decades, advancements in experimental methods, imaging capabilities and associated image analysis have awarded unprecedented insight into flow at the pore-scale [6,7]. It is now possible to observe—up to a time resolution of a few seconds and a spatial resolution of microns [8]—displacement at the pore-scale under a range of realistic conditions. Incorporating such rich experimental detail into a predictive framework has led to increased development of pore-scale models. With a wide variety of evolving models it is becoming increasingly important to identify the strengths that each modeling approach has and how they can

collectively further our understanding; however, thorough and quantitative pore-by-pore comparisons are still limited.

To date, some comparison studies have explored these matters for reactive-transport [e.g., Refs. [9–11]], while others have investigated macroscopic flow properties such as capillary pressure [12,13] and relative permeability [14]. Recently, Zhao *et al.* [15] analysed the macroscopic predictions of 14 pore-scale models, including DNS and PNM approaches, against benchmark quasi-2D micromodel experiments [16]. The authors found that no single approach could reproduce all of the experimental observations and that correctly incorporating fluid layers into simulations was profoundly challenging, particularly for DNS simulations which require tens, or even hundreds, of millions of lattice points to capture such features. Note that, in this paper, a distinction between fluid layers and films is made. Layers are wedges of wetting fluid retained in the corners of the pore space, whose thickness, typically of the order micrometers, is controlled by local pore geometry and capillary pressure [17]. Layers can allow significant flow. Films, in contrast, are of nanometer thickness, allow negligible flow and are controlled by intermolecular forces [18,19]. While films may affect surface properties, they do not directly contribute to the displacement processes described in this paper.

In direct simulations of pore-scale flow, Eulerian grid-based methods (finite-element, volume, or difference) [20,21] or particle-based methods (lattice-Boltzmann or smoothed particle hydrodynamics) [22–25] are used to numerically approximate the Navier-Stokes equations directly on the pore-space of a reconstructed 3D sample or an image. The appeal of

---

*luke.giudici@imperial.ac.uk

a high-fidelity approach is that few simplifications are made, allowing full consideration of viscous and capillary forces while preserving sample geometry, resulting in physically based predictive capabilities [26,27]. As such, DNS is vital to the characterization of pore and subpore behavior. However, the computational cost of performing such methods for multiple, high-resolution simulations at low capillary numbers renders DNS impractical for those without access to advanced computing power; even simulations on relatively small samples require CPU [22] or GPU [28] parallelization. Moreover, extending the use of high resolution DNS to the cm-scale, or to media exhibiting multiscale porosity, is an even greater challenge due to multibillion voxel image sizes. A complete understanding of pore-scale flow can only be achieved by exploring the parameter space on a representative elementary volume (REV), at similar capillary numbers present in the subsurface and at a resolution that captures important small-scale phenomena such as layer flow. Furthermore, macroscopic properties needed for upscaling should be obtained at the REV or above and ideally in a time and resource efficient manner. To achieve these requirements, simplifications to pore-space geometry and the governing equations are needed, leading to a network description of pore-scale flow.

Pioneered by Fatt [29], pore-network models provide a lower-fidelty approach which is fast, computationally efficient, and can handle sample volumes two orders of magnitude larger than DNS. PNMs discretize the pore-space into a topologically equivalent network—a lattice of pores connected by throats—through which flow is simulated semianalytically. The resulting decreased computational demands allow PNMs to simulate lower capillary numbers and the conceptual discretization of the system allows the inclusion of small-scale features, such as layer flow, to infinite resolution [30]. A simulation taking multiple weeks with DNS can be achieved on the order of minutes with a PNM, as shown later. However, the simplifications awarding PNMs such efficiency also bring disadvantages; the construction of a network replaces the true pore-space geometry with smooth, idealized elements which are often nonunique [31]. Further error is introduced due to semianalytic approximations to the governing equations.

To address the challenges associated with network modeling, the generalized network model (GNM) has been developed [32,33]. In classical network modeling, the pore-space is discretized into separate pores and throats based on a maximal-ball approach, with local maximal and minimal inscribed spheres representing pores and throats, respectively [34]. The pores and throats are then assigned idealized, nonunique geometric shapes with the same shape factor as the underlying image. The GNM adopts a new approach: the corners of the pore-space between any two connected pores are discretized and used as the main elements of the network. This richer geometric characterization better preserves subpore features and removes the nonuniqueness of classical network elements, moving closer to a first-principles predictive approach. Ultimately, the GNM aims to be an upscaled representation of the pore and subpore physics captured by DNS, while allowing a greater number of physically based parameters relative to classical PNMs. Extensive calibration and comparison with DNS is needed to ensure that semianalytic

approximations and physically based correlations in the GNM are accurate, and that macroscopic properties, such as capillary pressure, and local properties, such as occupancy and saturation, are consistent between the two modeling approaches.

Successful development of a network model that incorporates sample geometry, captures the upscaled behavior of DNS, and retains the desirable efficiency of PNMs would provide a powerful predictive tool. The objective of this paper is to develop a workflow to compare two-phase flow predictions from a color-gradient lattice-Boltzmann DNS model and the GNM, on both a macroscopic (capillary pressure) and local (saturation and occupancy) basis. A quantitative, pore-by-pore comparison between the models is then presented for Bentheimer sandstone and a synthetic beadpack, through a full range of wetting states, in addition to comparisons with experimental data for Bentheimer sandstone. The workflow provides insights into the relative strengths and shortcomings of each approach and seeks to analyze the difference in pore-scale behavior between the GNM and higher-fidelity approaches.

II. MATERIALS AND METHODS

A. Generalized network model

The generalized network extraction algorithm [32] is used to discretize the void-space in a micro-CT image into individual pore and throat elements of a network. Pore centers are defined as local maxima of the distance map—a scalar field of the distance between each void voxel and its nearest solid voxel—while throats are defined as the narrowest restriction between two adjacent pores. Every void voxel in a micro-CT image is assigned to a unique pore and throat element. These pores and throats are used to validate local fluid properties, such as saturation and occupancy, between the GNM and DNS. An indicator function, α, is used to determine the occupancy of a pore or throat: $\alpha = 0$ if the voxel nearest the center of a pore or throat is filled with water, while $\alpha = 1$ if it is filled with oil. Saturation is computed as the fraction of voxels filled with a fluid phase (α) in any given element and can take values $S_\alpha \in [0, 1]$.

The generalized network then differs from classical approaches; the throats are further divided along their medial axis into corners. Discretizing in this way preserves the underlying topology while retaining a rich geometric description of the pore-space, as the corners' geometric parameters are acquired directly from the underlying image. The single-phase permeability of the sample is preserved via an upscaling of the Navier-Stokes equations solved directly on the image.

Quasistatic, capillary dominated two-phase flow is simulated through the extracted network using the generalized network flow model [33]. Improvements in the calculation of threshold capillary pressure accounting for the sagittal curvature of fluid menisci are implemented, as described by Giudici *et al.* [35]. Displacements are driven by incrementally increasing the invading phase pressure at the inlet, with fluid interface locations updated in accordance with capillary equilibrium in each pore or throat:

$$P_c = P_o - P_w = \sigma \kappa, \tag{1}$$
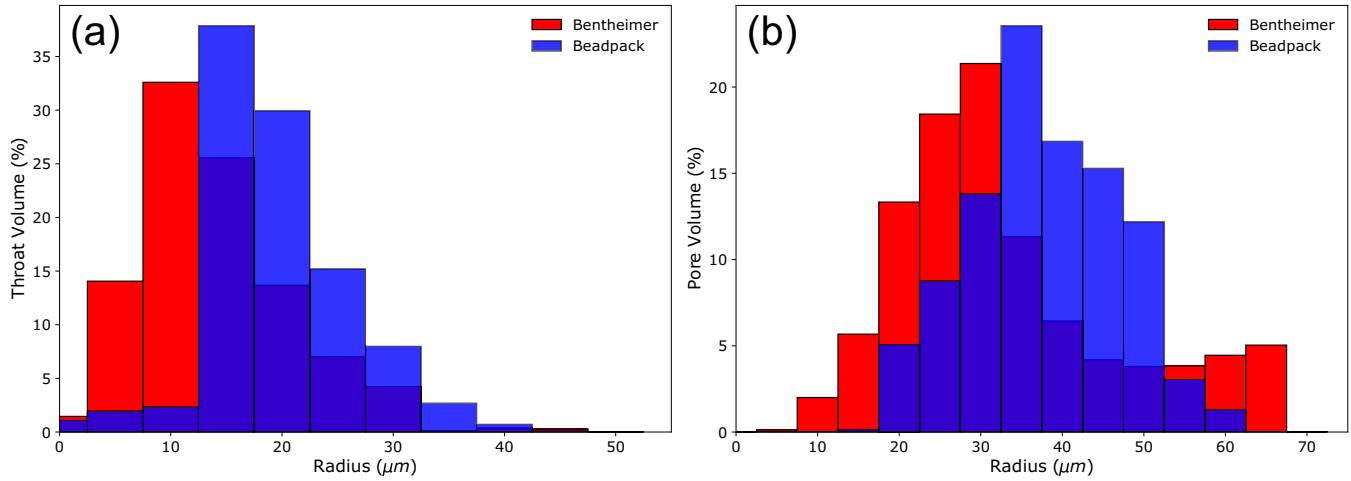
FIG. 1. The pore-volume weighted radius distributions for throats (a) and pores (b). The red bars represent Bentheimer and the blue bars represent the synthetic beadpack.

where P_c is the capillary pressure, P_o and P_w are the fluid pressure of oil and water, respectively, σ is the interfacial tension, and κ is the total curvature of the interface. Layer growth, snap-off, and layer collapse are simulated by tracking the three-phase contact lines as fluid interfaces move through pores and throats. After a user-defined change in network saturation, set to 1% in this work, the conductivity of each corner is calculated and averaged to provide the conductivity of each throat. Subsequently, a mass balance on each pore, p, is invoked to determine the flow rate in each throat, t:

$$\sum_{t \in p} q_t^\alpha = \sum_{t \in p} g_t^\alpha (\Phi_p - \Phi_{\text{nei}}) = 0, \quad (2)$$

where q_t^α is the total flow rate of a phase (α) passing through a throat (t), g_t^α is the throat conductivity, and $\Phi_p - \Phi_{\text{nei}}$ is the viscous pressure drop between neighboring pores. The summation is over all throats connected to a given pore. Simulations in this work assume capillary dominated displacement, with $\sigma = 0.025 \, \text{Nm}^{-1}$.

B. Direct numerical simulations and samples

Two-phase flow predictions obtained with the GNM are compared to those generated in Akai *et al.* [36] using a recently developed lattice-Boltzmann model (LBM). Below, the method used to obtain LBM predictions is briefly described; for a complete treatment of the reader is referred to Akai *et al.* [37].

Two-phase flow simulations on two 288^3 voxel samples—a synthetic beadpack and a micro-CT imaged Bentheimer sandstone, both with a voxel size of $3.58 \, \mu\text{m}$—were performed using a color gradient lattice-Boltzmann model by Akai *et al.* [36]. Although small, this size is likely large enough to be considered a representative elementary volume for a Bentheimer sample [38,39] and hence also for the beadpack, as its pore-space is more homogeneous than Bentheimer. The pore-radius distribution for both samples is shown in Fig. 1. Initially, drainage simulations were performed with a uniform contact angle, θ, of 45° by increasing the oil pressure, relative to the water pressure, and applying constant pressure boundary conditions at the inlet and outlet. Following

primary drainage, water injection was simulated for three wetting states in each sample: uniformly water-wet (WW, $\theta = 45°$), uniformly oil-wet (OW, $\theta = 135°$), and a mixed-wet (MW) state exhibiting a nonuniform allocation of contact angle—the contact angle assigned at the start of waterflooding was positively correlated with the oil saturation of pores after drainage, mimicking wettability alteration in realistic settings. The contact angles assigned after drainage in the MW case ranged from 45° to 165°, with a volume-weighted average of 90°. Each waterflood was initiated from the same drainage simulation. All simulations were in a capillary dominated regime, with an average capillary number Ca $< 10^{-5}$ during the displacements.

Using a no-slip boundary condition, at least three grid blocks are required at the solid-wall to capture fluid layers using DNS. Furthermore, Zhao *et al.* [40] suggested that at least 10 grid blocks across the diameter of a throat are needed for LBM P_c predictions to lie within 5% of analytic values, and insufficient mesh resolution has an adverse effect on relative permeability predictions [14]. The grid size used in the simulations here was $3.58 \, \mu\text{m}$. Figure 1 shows that the volume-average pore and throat diameter (μm) is 66 and 28 for Bentheimer, and 76 and 38 for the beadpack, respectively. With a grid size equal to the voxel size of $3.58 \, \mu\text{m}$ these values correspond to $\sim$10 grid blocks per throat and $\sim$20 grid blocks per pore. Note that this is the volume-average resolution—some throats in Fig. 1 will have fewer grid blocks per diameter, particularly for Bentheimer. In this work, experimental capillary pressures will be presented to validate model predictions and, to avoid resolution errors, pore-by-pore analysis excludes the throats. The main implication, however, is that layer flow cannot be simulated by the LBM at this resolution. It is important to emphasize that this is not indicative of an inability of LBM to model layers as a whole; indeed, many studies have successfully modeled wetting layers, and even thin films, in simple systems using color-gradient, interparticle potential, free-energy, mean-field, and stable-diffuse interface LBM schemes [e.g., Refs. [41–46]]. However, there is an inherent trade-off in all schemes between the resolution of the simulation domain and the physical volume of the
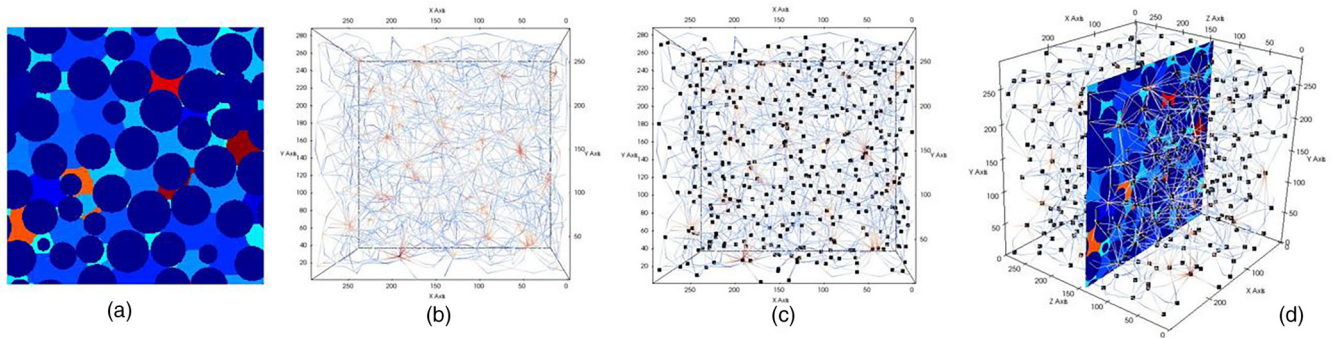
FIG. 2. The steps implemented to obtain a spatial match in wettability between models. The pore regions identified by Akai *et al.* [36] are shown in panel (a). The generalized network is shown in panel (b), with the pore centers represented by black squares in panel (c). Finally, each pore center in panel (c) is mapped to a pore region in panel (a), shown in panel (d). After mapping, wettability assignment is easily transferred between models.

sample modeled. For many media, particularly if the structure and porosity are heterogeneous, the representative size may be cubic millimeters or centimeters in volume. Achieving micrometer resolution in such volumes is extremely demanding, leading many studies to omit small-scale features in more complex media [e.g., Refs. [23,38,47,48]]. As shown later, this omission can have significant impacts on macroscopic predictions of trapping and pore-by-pore displacement characteristics.

C. Assignment of contact angle

The generalized network extraction algorithm differs from the method used in the LBM study by Akai *et al.* [36] in how the pores are identified. In the water-wet and oil-wet cases this is inconsequential as the wettability assignment is uniform. The mixed-wet cases, however, require a spatial match in contact angle. This is achieved by implementing the steps shown in Fig. 2. A generalized network is extracted from the images used in Akai *et al.* [36]. The pore centers in the generalized network model are then overlaid onto the pore regions used in the LBM study. Finally, the contact angle associated with each pore-region in the LBM study is mapped to the pore-center(s) of the network model. In this way, the spatial distribution of contact angle is matched as closely as possible between models—Fig. 3 compares the distribution of contact angles as a function of pore-volume, in the mixed-wet case, for both samples. The distributions are similar, with only a 1° and 2° difference in the volume-weighted average of contact angle for Bentheimer and the beadpack, respectively. Network flow simulations were performed after the contact angle was assigned pore-by-pore to closely match those of the LBM study, and a series of macroscopic and pore-by-pore comparison measures were implemented on the model predictions.

D. Comparison measures

To compare the higher-fidelity DNS model and the GNM, a series of qualitative and statistical measures are implemented on both a macroscopic and a pore-by-pore basis, explained below.

1. Macroscopic mismatch

Capillary pressure [Eq. (1)] is used to qualitatively determine the similarity between the two modeling approaches at a macroscopic scale. Capillary pressure is dependent on pore geometry, wettability, saturation and the invading phase history (capillary pressure hysteresis). Hence, differences in P_c provide important insights into pore-scale displacement. The capillary pressure for drainage and each waterflood, for both models, are shown for Bentheimer and the beadpack. For the Bentheimer sandstone, experimental observations for drainage, water-wet waterflooding [49], and mixed-wet waterflooding [50] are presented for comparison, with an updated quantification of uncertainty by Foroughi *et al.* [51].

Another macroscopic measure used is the Pearson correlation coefficient, r, which is a measure of the linear relationship
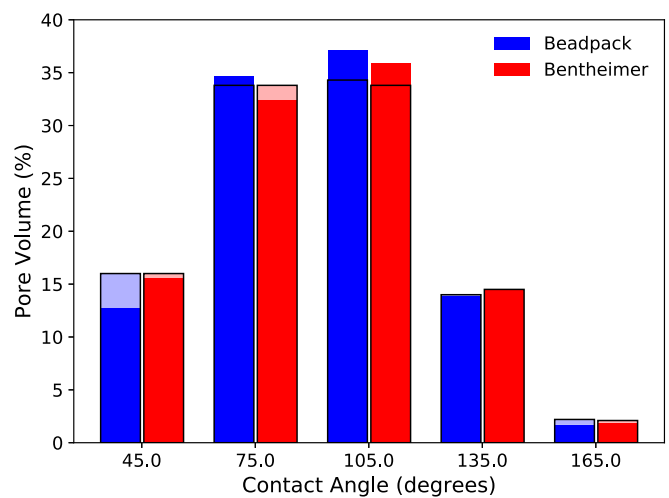
FIG. 3. The contact angles assigned to the pore volume of the mixed-wet case, prior to waterflooding, for the GNM and the Akai *et al.* [36] LBM study (pale bars outlined in black). The volume-weighted average contact angle is 90° in the LBM study while it is 91° and 92°, for the Bentheimer and beadpack, respectively, in the GNM.
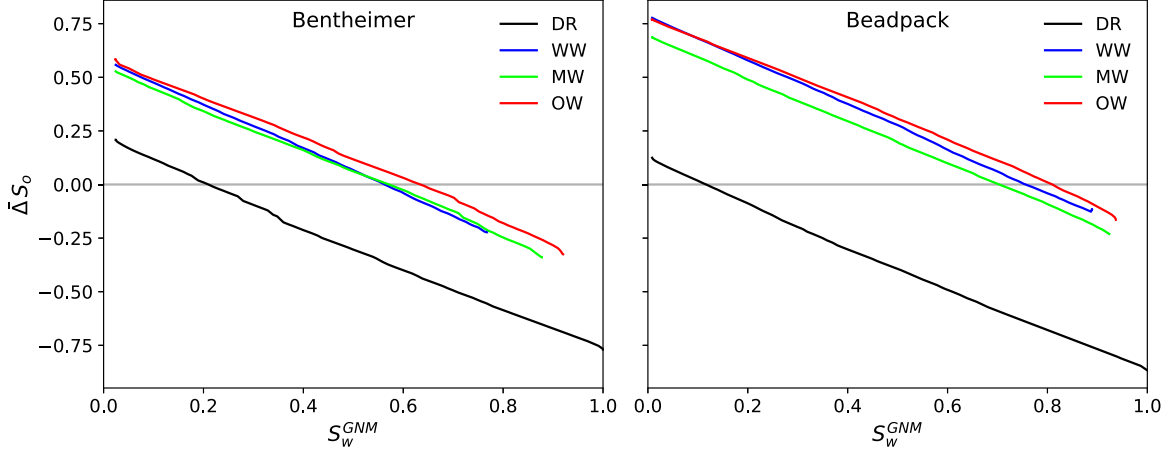
FIG. 4. The method used to establish the comparison points between two models. Flow simulations of four regimes are compared: primary drainage (DR) and water-wet, mixed-wet, and oil-wet waterflooding (WW, MW, and OW, respectively). In each simulation, the total water saturation of the GNM network (S_w^{GNM}) is increased incrementally by 1%. At each saturation increment in the GNM, the mean difference in pore saturation of oil ($\bar{\Delta} S_o$) between the prevailing state of the GNM network and the end state of the LBM is calculated [Eq. (4)]. The total network saturations at which the two models are compared is given by the intersections of the lines with $\bar{\Delta} S_o = 0$—for each wetting regime, the models are compared when their mean pore saturations are equal.

between two datasets and is defined as

$$r = \frac{\sum_{i=1}^{n} \left(\psi_i^a - \bar{\psi}^a \right)\left(\psi_i^b - \bar{\psi}^b \right)}{\sqrt{\sum_{i=1}^{n} \left(\psi_i^a - \bar{\psi}^a \right)^2} \sqrt{\sum_{i=1}^{n} \left(\psi_i^b - \bar{\psi}^b \right)^2}}, \quad r \in [-1, 1],$$

(3)

where ψ_i^a and ψ_i^b are the ith members of two datasets, a and b, with mean values $\bar{\psi}^a$ and $\bar{\psi}^b$, and n is the sample size. The Pearson correlation coefficient between saturation and radii, and occupancy and radii, is calculated at the end of drainage and each waterflooding cycle for the LBM predictions (r_{LBM}), and compared to the correlation coefficients calculated for the network model predictions (r_{GNM}) when the mean difference in the models' pore-saturation is zero (detailed in Sec. II D 2) and the wettability is the same. This comparison determines the degree to which the models agree in terms of their invasion behavior—similar coefficients indicate agreement in the invasion trends (i.e., are large or small pores preferentially filled) and in variance of the prediction. A value of -1 indicates perfect negative correlation and a value of 1 indicates perfect positive correlation, while 0 indicates no correlation. As wettability assignment is equal in both models, a large disparity in the Pearson correlation coefficient reflects differences in the invasion algorithm and treatment of pore-space geometry.

Finally, the residual saturation after waterflooding, S_{or}, is primarily controlled by the amount of trapping due to snap-off and the presence of flow through layers, which in turn are controlled by the wettability of the system. It has important implications for oil recovery and CO_2 storage [52,53]. S_{or} as a function of wettability is presented as a measure of the macroscopic differences manifesting from the treatment of small-scale phenomena and model resolution.

2. Pore-by-pore mismatch in occupancy and saturation

LBM predictions at the end of drainage and the end of waterflooding are first mapped onto pore-network elements,

in a similar fashion to contact angle (Fig. 2), enabling pore-by-pore comparison between models. The mean difference ($\bar{\Delta}$) and mean absolute differences ($|\bar{\Delta}|$) between model predictions for occupancy and oil saturation (the fraction of the volume of a pore filled with oil) are then calculated, as in Raeini *et al.* [54]:

$$\bar{\Delta} \psi = \frac{\sum_{i=1}^{n} w_i \left(\psi_i^a - \psi_i^b \right)}{\sum_{i=1}^{n} w_i},$$

(4)

$$|\bar{\Delta}| \psi = \frac{\sum_{i=1}^{n} w_i \left| \psi_i^a - \psi_i^b \right|}{\sum_{i=1}^{n} w_i},$$

(5)

where ψ represents any flow parameter, such as saturation or occupancy, for two data sets a, b while w_i is a weighting factor—chosen here to be the pore volume. Equation (4) can be considered the difference in the average, upscaled flow parameter, as local differences between models can cancel, while Eq. (5) represents a true pore-by-pore difference—it is the normalized sum of pore-by-pore discrepancy. A difference here indicates disagreement in the models' invasion algorithms, pore-space geometry and incorporated physics—as in Eq. (3)—but provides a direct measure of the local disagreements. Both pore-by-pore comparison measures are determined when the mean difference in pore saturation [Eq. (4)] between the GNM and the saturation at the end of LBM drainage, or waterflooding, is zero (Fig. 4).

III. RESULTS AND DISCUSSION

In Sec. III A the GNM and LBM are quantitatively compared at the macroscopic scale, using the methods described in Sec. II D 1, to determine the average behavior of each model. Experimental measurements of capillary pressure in Bentheimer [49,50,55] are also used to aid macroscopic comparison. Subsequently, in Sec. III B, the local differences between models are analysed using the methods described in Sec. II D 2.
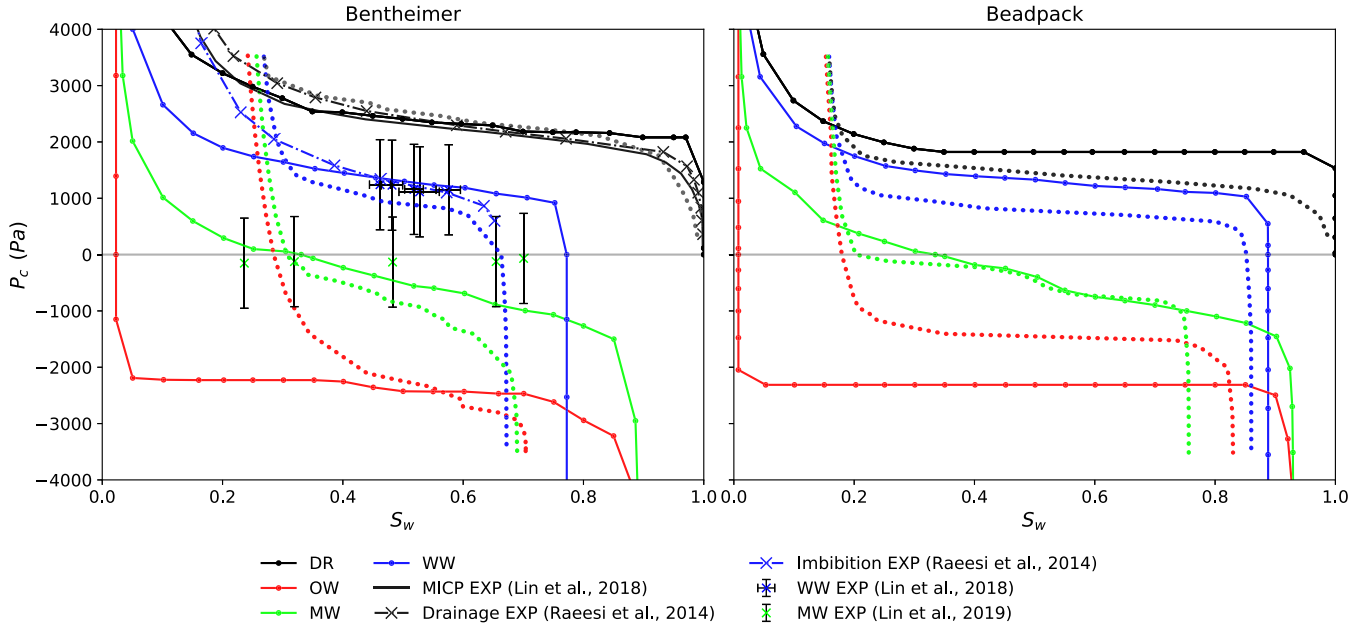
FIG. 5. Capillary pressure (P_c) comparison between the LBM (dotted lines) and the GNM (solid with dots), for a beadpack and Bentheimer sandstone. In each plot, the colors distinguish primary drainage and water-wet, mixed-wet, and oil-wet waterflooding (DR, WW, MW, and OW, respectively). For the Benthiemer, experimental results (EXP) from Raeesi *et al.* [55], Lin *et al.* [49], and Lin *et al.* [50] are superimposed with error bars indicating the uncertainty in the measurements [51].

A. Macroscopic comparison

In the context of reservoir simulation, the two major up-scaled flow-properties needed as an input into field-scale models are capillary pressure and relative permeability. Any modeling approach intended for practical use needs to accurately reproduce these properties. The focus in this paper is on the former of these properties, as an analysis of relative permeability was not performed by Akai *et al.* [36]. The wettability of the models is matched on a pore-by-pore basis; differences in P_c are due to representation of the pore-space geometry or the dynamics of the invasion. Akai *et al.* [36] compared their LBM results against a water-wet experiment by Raeesi *et al.* [55], in which capillary pressure was measured using the porous-plate method. Their comparison showed good agreement with the experiment, slightly overpredicting drainage and underpredicting imbibition capillary pressure. A comparison between GNM, LBM and experimental capillary pressures—obtained with the porous plate [55] and micro-CT image curvature measurement [49,50] methods—is shown in Fig. 5.

The LBM shows an initial water saturation (S_{wi}) after primary drainage of 27% and 16%, for Bentheimer and the beadpack, respectively. Experimental observations, however, exhibit around $S_{wi} = 10\%$ for Bentheimer and $S_{wi} = 6$–10% for a packing of smooth beads [56], although the presence of surface roughness can reduce this to $S_{wi} = 1\%$ or less [57]—far lower than predicted by the LBM. In contrast, the GNM reaches lower S_{wi}'s than LBM—less than 5% in both samples—and better agrees with experimental findings. The cause of this discrepancy is the computational difficulty for LBM, and indeed all direct numerical simulations, to perform simulations at a resolution necessary to capture layer

flow. Without wetting layers to sustain water-connectivity to the outlet throughout drainage, the wetting phase becomes surrounded and trapped.

The resolutions needed to capture layer flow (a minimum of three grid blocks) significantly increases simulation time, and the flow rates necessary to simulate layer flow may result in viscous-dominated behavior. While high performance computing is extensively used in LBM studies, providing the means to capture layers, each simulation still typically takes on the order of days to weeks to complete. For reference, each GNM drainage-waterflood cycle shown in Fig. 5 took 1 minute using a single core with a clockspeed of 2.30 GHz and a floating point operations per second (FLOPS) rating of 3.6 GFLOPS. In contrast, the LBM simulations—without layers—took on the order of two weeks using 128 cores with a clockspeed of 2.5 GHz and a numerical performance rating of 3.1 GFLOPS per core. This corresponds to approximately six orders of magnitude difference in computational time between the generalized network model and the LBM.

Due to these computational challenges associated with direct simulations, layer flow is often omitted from LBM studies, leading to an overestimation of trapped water saturation after primary drainage. It is important to emphasize that the remaining water is truly trapped—it is not connected to the outlet via wetting layers, as seen in experiments [17,58,59]. In comparison, the generalized network model is able to simulate complete primary drainage; the wetting phase remaining in the network following drainage is rarely disconnected from the outlet as thin wetting layers maintain connectivity, even at very high capillary pressure, through the corners of the pore-space. As layers are conceptually incorporated, rather

than explicitly modeled, their inclusion comes at little extra computational cost and the resolution is the same as the precision of the hardware used for the simulation.

The oil-wet case in Fig. 5 shows large P_c discrepancy between the GNM and LBM predictions, in both the Bentheimer and beadpack, for the majority of the displacement. This is related to the inability of the LBM to reach low initial saturations at this resolution, as explained above. During drainage, oil preferentially invades the pore space in order of size, from largest to smallest, in accordance with growing capillary entry pressure [18]. The smallest regions of the pore-space are the most difficult to invade—only a high capillary pressure can push the nonwetting phase into these regions. In the LBM, the wetting phase will never leave these regions. The nonwetting phase will find other, easier paths and leave the wetting phase trapped and disconnected in small crevices. Subsequently, an oil-wet wettability alteration occurs and water is injected, which has now replaced oil as the nonwetting phase. The pore-space is once again invaded in decreasing order of size. However, in the LBM, the smallest regions—those which require the highest water pressure, and hence the most negative capillary pressure—remain occupied with water. Thus the nonwetting phase (water) can span the system without displacing through narrow, high entry-pressure regions. In the GNM, this is not the case. The capillary pressure and connectivity necessary to fully drain the sample during primary drainage are achievable, resulting in the smallest regions of the pore-space becoming occupied with the nonwetting phase. Subsequently, injected water must displace oil from these narrow regions if it is to span the system. The capillary pressure immediately reaches large, negative values to achieve this. The narrow range of pore-size distribution shown in Fig. 1 accounts for the flat capillary pressure throughout the remaining displacement—once the narrowest region is invaded, the nonwetting phase pressure is sufficient to percolate through the rest of the system.

The mixed-wet case in Fig. 5 reveals insights into the nature of displacement in both models. Both models show good agreement within ∼40–70% water saturation, beyond which the impact of oil-layer flow becomes apparent, as discussed later. Indeed, for Bentheimer both models lie within the uncertainty of experimental observations [50] during intermediate saturations, with the GNM closer overall. However, the key observation highlighting the differences between the models lies in the early stages of displacement, $S_w < 40\%$. The LBM shows an almost vertical decrease to negative capillary pressure at the start of waterflooding—there is little spontaneous displacement and the invading phase must be forced into the pore-space. From the contact angle distribution (Fig. 3) it is evident that there are water-wet regions of the pore-space. Indeed, the GNM predicts significant spontaneous displacement at positive capillary pressures and spontaneous imbibition in mixed-wet samples has been experimentally observed [60]. The cause of this difference is again the absence of wetting layers connecting trapped water to the inlet at the end of drainage, discussed previously.

Upon injection of water, wetting layers swell throughout the pore-space until their arc menisci reach a critical radius of curvature, beyond which the narrowest, water-wet regions of the pore-space are spontaneously filled. These narrow regions

of the pore-space can then act as nucleation points for displacement in adjacent, less water-wet pores and throats. This is ordinary percolation [18]. The LBM, however, is not able to access these water-wet regions of the pore-space. Invasion must progress as invasion-percolation, in which elements are only invaded if they are connected to the inlet through the center of the pore-space. As much of the pore-space in the mixed-wet case has experienced wettability alteration and displacement is invasion percolation-like, to form a connected pathway across the sample, oil-wet regions of the pore-space must be invaded, causing the capillary pressure to become negative. The difference in percolation behavior is evident from Fig. 6, which shows the contact angle of newly invaded regions as a function of saturation.

The contact angles in this study are known exactly and are spatially matched in both models (Fig. 2), allowing in-depth pore-by-pore analysis. Both models in Fig. 6 show general agreement in their volume-averaged behavior (solid lines), with more water-wet regions invaded before oil-wet; however, the range of contact angles invaded (shaded area) is significantly different. For $S_w < 60\%$, the GNM predicts that displacement predominantly occurs in the more water-wet regions of the pore-space, accounting for displacement at positive capillary pressure in the network model shown in Fig. 5. The most oil-wet regions are not invaded until the final stages, for water saturations above ∼60%. In the LBM, however, the invading phase has no choice but to push through oil-wet regions as it cannot percolate into water-wet regions without terminal menisci first reaching them, as shown by the immediate increase in volume-average contact angle followed by a sharp drop in Fig. 6. This fluctuating behavior is seen throughout the LBM simulations, and is most apparent in the Bentheimer sandstone due to its lower pore-space connectivity. In addition, the LBM exhibits a consistently higher invaded maximum contact angle until the final stages of waterflooding—the most oil-wet regions are always invaded, regardless of S_w, whereas these regions are bypassed in the GNM as favourable water-wet regions are accessible via wetting layers. The apparent absence of ordinary percolation-like behavior in the LBM could have important implications for future modeling of mixed-wet systems. While direct numerical simulations are undoubtedly successful for high resolution, physics-based studies of flow using massively parallel processing, time and resource-efficient simulations with true predictive capability for mixed-wet systems—able to incorporate small-scale flow phenomena and the associated displacement phenomena on representative sample sizes—may be better suited to network modeling.

Thus far, the macroscopic comparison has highlighted differences caused by the absence of wetting layers in the LBM at the resolution of the simulations. However, wettability alteration can also cause the formation of oil layers in the corners of the pore-space, as seen experimentally [61]. At the end of drainage, water is retained in the corners of the pore-space and exists as wetting layers, while the solid surface bounding the center of a pore region is contacted by oil and subject to wettability alteration [62]. During waterflooding, water (now the nonwetting phase) occupies the center of the pore-space and leaves oil as a stable layer between the water occupied corners and center. These layers allow the oil to escape even
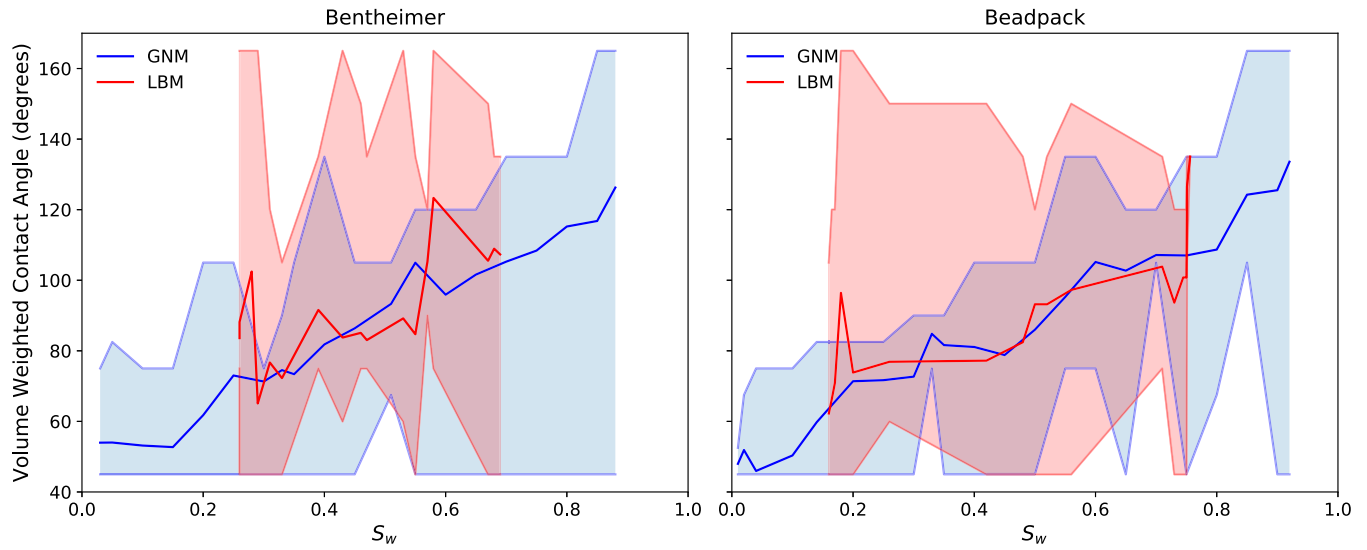
FIG. 6. The contact angles of newly invaded elements during waterflooding in the mixed-wet case as a function of water saturation (S_w). The generalized network model is shown in blue while the lattice-Boltzmann model is shown in red. Solid lines represent the volume-average, while shaded regions show the range of invaded contact angles.

if the center of the pore-space is blocked. The stability of oil layers is determined by the pore geometry and the initial water saturation—angular pore-spaces with lower initial water saturation have thicker, stabler oil layers—but in general their existence allows altered wettability media to reach low residual oil saturations.

Figure 7 shows the residual saturations predicted by both models for both samples. The beadpack has a better connected pore-space and shows lower residuals than Bentheimer, but the network model predicts far lower residuals than the LBM in both samples. The principal reason for this is the inclusion of oil-layer flow in the GNM. While it is true the GNM waterflooding simulations begin with a lower S_{wi}, and hence

stable oil-layer flow throughout the simulation is expected, the impact of wettability alteration on residual oil is entirely missed by the LBM due to the computational constraints of modeling small-scale features with a resolution of 3.58 μm. In the beadpack, the LBM predicts the minimum trapping of oil to be the water-wet case. Cooperative pore-body filling dominates in water-wet scenarios, leading to efficient sweep of the nonwetting phase out of the medium, and without the presence of wetting layers to facilitate snap-off there will be minimal trapping. For mixed-wet (without ordinary percolation) and oil-wet conditions, piston-like advance is dominant and the finger-like growth of the invading phase can trap large clusters of the defending phase in small regions. The manifestations
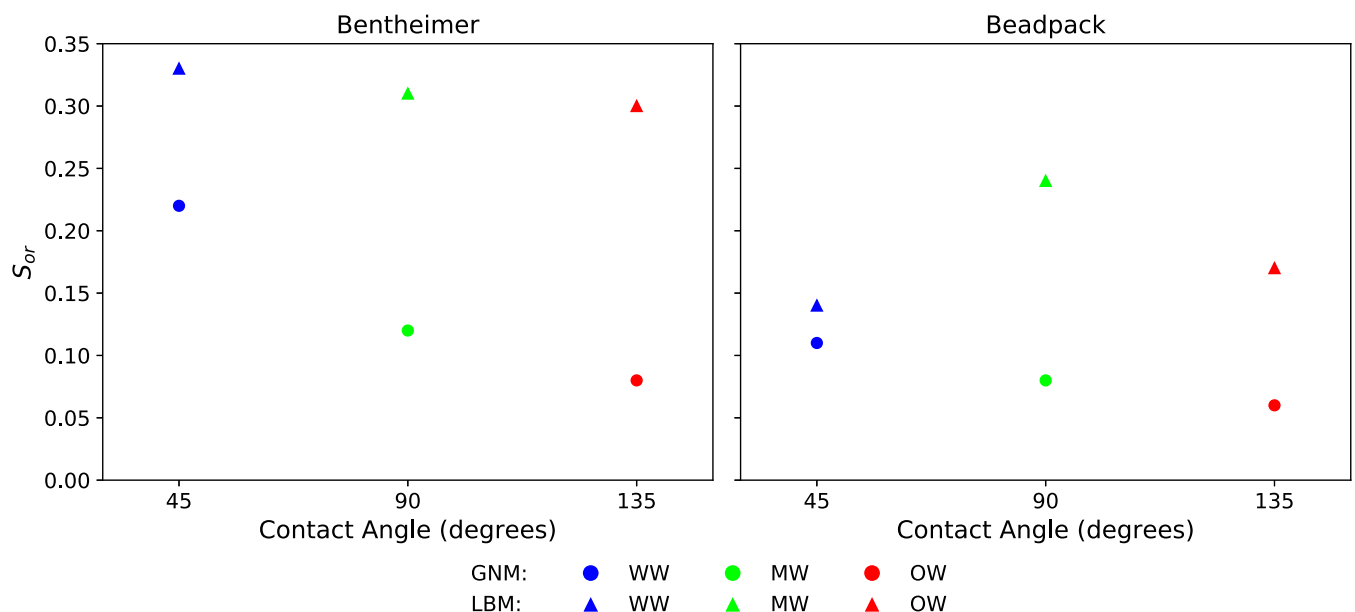
FIG. 7. Residual oil saturations (S_{or}) after waterflooding predicted by the GNM (circles) and LBM (triangles) for the simulated water-wet, mixed-wet and oil-wet wettabilities (WW, MW, and OW, respectively).
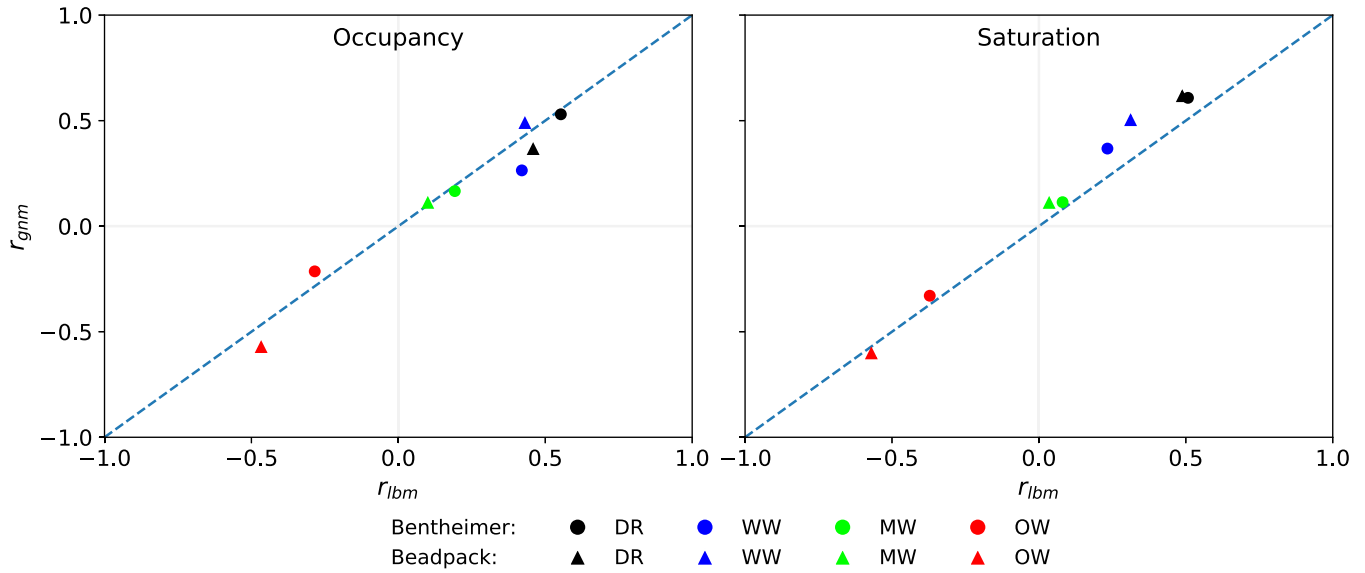
FIG. 8. The Pearson correlation coefficients, r [Eq. (3)], of occupancy and oil-saturation with radius predicted by the GNM and LBM models after primary drainage and water-wet, mixed-wet and oil-wet waterflooding (DR, WW, MW, and OW, respectively). Triangles and circles represent predictions for the beadpack and Bentheimer, respectively, and the color of the data points corresponds to their wettability.

of these displacement processes is not evident in the LBM Bentheimer predictions in Fig. 7 because the pore-space is not as well connected—if a few key throats are invaded, the exit of oil will be blocked, while in the beadpack there will still be pathways to escape—and hence there is little variation in LBM Bentheimer residuals as wettability changes from water-wet to mixed and oil-wet states. The GNM does capture the effect of oil-layer flow and the varying displacement dynamics, predicting that the residual oil saturation decreases with an increase in average contact angle, as seen experimentally [63–65].

The inclusion of layer-flow has a clear impact on the nature of pore-scale displacement and the model predictions thus far, but at a macroscopic level it is useful to determine whether the models observe similar displacement sequences—that is, do the models predict the same fluid movement in the pore-space. Despite the shortcomings of LBM, it is mathematically closer to a first-principles approach than network modeling and hence it is important to ensure the semianalytic approximations present in the GNM reproduce the upscaled-behaviour of direct methods. Figure 8 compares the Pearson correlation coefficients of radius with occupancy and oil saturation for both models, with the dotted blue line corresponding to an exact agreement. Both models indicate strong, positive correlation of occupancy and saturation with radius during drainage and water-wet waterflooding, as observed experimentally [60,66,67]. Likewise, both models agree in the mixed-wet case where only a slight positive correlation in occupancy and saturation with inscribed radius is present, again as confirmed experimentally [60,68]. Little correlation is expected as the volume-averaged contact angle is $90°$, with a range of contact angles above and below as shown in Fig. 3, and hence both imbibition and drainage are occurring simultaneously. Although small, the observation of positive coefficients in the mixed-wet cases can be explained as follows: during drainage, oil will occupy the largest regions

of the pore-space first. This will result in a positive correlation of saturation with radius at the end of primary drainage, as shown in Fig. 8. The degree of wettability alteration in both models is akin to that seen in experiments: pores highly saturated with oil experience stronger wettability alteration. Thus, at the beginning of waterflooding, large pores are occupied with oil and are more oil-wet than small pores, which retain more water and experience less alteration. It is almost always easier for water to invade the smaller, water-wet regions rather than the larger, oil-wet regions (Fig. 6) resulting in a positive correlation of oil-occupancy and saturation with radius. This behavior has also been noted experimentally [69]. In the oil-wet case, if the oil-wet state is considered analogous to drainage with the invading and receding phases swapped, a negative correlation of occupancy and saturation with radius is again self-explanatory and has been observed experimentally [70]. In summary, Fig. 8 indicates that the GNM exhibits the same upscaled behavior as the LBM and experiments.

B. Pore-by-pore comparison

The pore-scale configuration and connectivity of fluids ultimately controls the upscaled macroscopic properties of interest to field-scale simulations. The exact pore-scale configuration of fluids is not even completely reproducible between repeat experiments on the same sample [54]—the mean and mean absolute difference for simple sandstones and carbonates can be as large as 8% and 17%, respectively. These pore-by-pore discrepancies therefore represent the closest agreement between model and experiment possible with the use of experimental constraints on input parameters. However, repeat experiments closely agree in upscaled properties and thus it is assumed that if the mean and mean absolute differences between model and experiment—or indeed two models—are similar to the discrepancy between repeat experiments, the upscaled properties should also be simi-
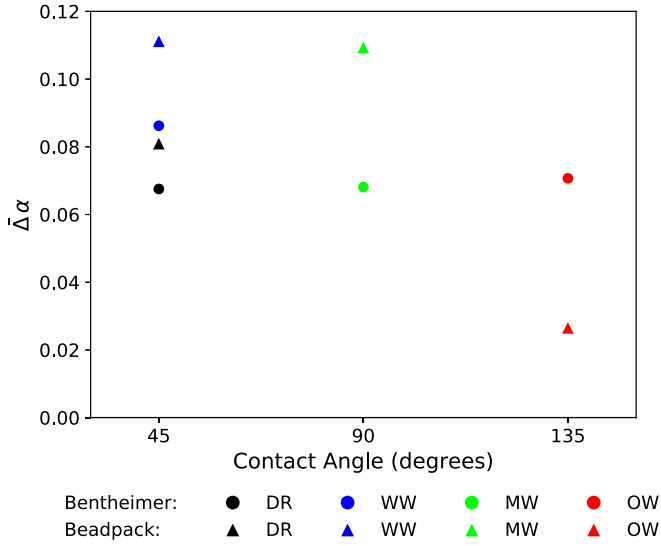
FIG. 9. The mean difference [Eq. (4)] in occupancy ($\bar{\Delta}\alpha$) between the GNM and LBM for all simulations performed. The colors indicate wettability, while circles and triangles represent the Bentheimer and beadpack, respectively.

lar. For instance, the GNM showed moderate pore-by-pore agreement with water-wet experiments in both Bentheimer sandstone [71,72] and Ketton limestone [71,73], with a mean difference of ~10% and a mean absolute difference of ~30% [54], while upscaled predictions agreed well with experimental measurements in water-wet Bentheimer [33,35].

Figure 9 shows the mean difference in pore occupancy between the GNM and LBM as a function of wettability, while Fig. 10 shows the absolute difference in pore occupancy and saturation as a function of wettability, for both the Bentheimer and beadpack samples. The mean difference in saturation (not shown) is zero, as outlined in Fig. 4. To quantitatively assess the absolute differences between modeling approaches, a reference is needed. The expected absolute difference in oil saturation between two networks randomly saturated with a

fraction, S_o, is given by [51]

$$E(|\bar{\Delta}|S_o) = 2S_o(1 - S_o). \quad (6)$$

Equation (6) is used to normalize the absolute values of saturation obtained using Eq. (5). However, two identical media with the same mean saturation (Fig. 4) do not necessarily have the same occupied fraction, p. Thus, for two identical media A and B, the expected absolute difference in occupancy assuming random filling is given by

$$E(|\bar{\Delta}|\alpha) = p_A(1 - p_B) + p_B(1 - p_A), \quad (7)$$

where p_A and p_B represent the fraction of occupied elements in A and B, respectively. The absolute differences in occupancy presented in Fig. 10 are normalized by Eq. (7).

The mean difference in pore occupancy shown by Fig. 9 is small and consistent with experimental comparisons. Physically, this means that the GNM predicts the average, upscaled occupancy to within 11% of both a higher-fidelity LBM and experimental observations—all three approaches agree. It is evident that the mean differences are positive, which indicates that more of the pore-space is occupied with oil in the GNM for any given water saturation. This is a direct manifestation of the nature of displacement in the two models: in the GNM, a change in saturation can arise from a change in volume of the wetting layers, leaving the occupancy unaltered. In the LBM, however, the absence of wetting layers results in pore occupancy accommodating saturation changes. This discrepancy in model behavior is also shown in the mean absolute differences (Fig. 10), where there are a number of observations to note.

First, the normalized mismatch in predictions decreases with increasing contact angle in both samples. This observation is due to the relative prevalence of ordinary percolation in combination with the order of filling, and is closely linked to the findings shown in Figs. 6 and 9: invasion is limited to invasion percolation in the LBM, and saturation changes cannot be attributed to wetting layers. In water-wet regimes, filling proceeds in order of increasing size in an ordinary percolation-
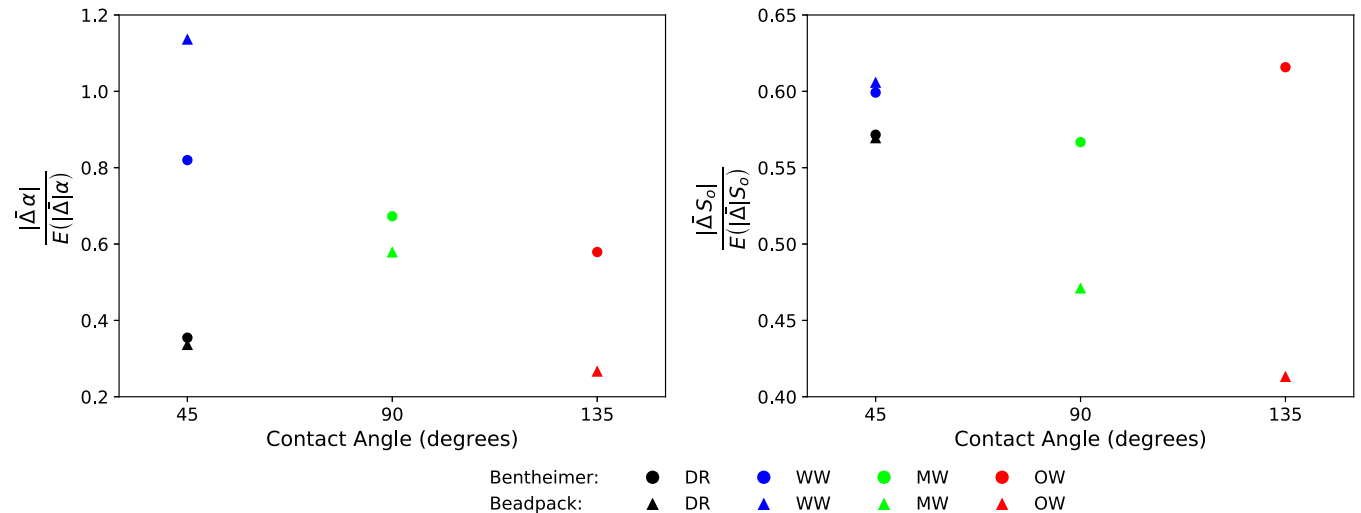
FIG. 10. A comparison of the absolute differences [Eq. (5)] in pore occupancy ($\bar{\Delta}|\alpha$) and pore oil-saturation ($\bar{\Delta}|S_o$) between models, normalized by the expected absolute differences [Eqs. (6) and (7)], after primary drainage and water-wet, mixed-wet and oil-wet waterflooding (DR, WW, MW, and OW, respectively). The circles and triangles represent the Bentheimer and beadpack samples, respectively.
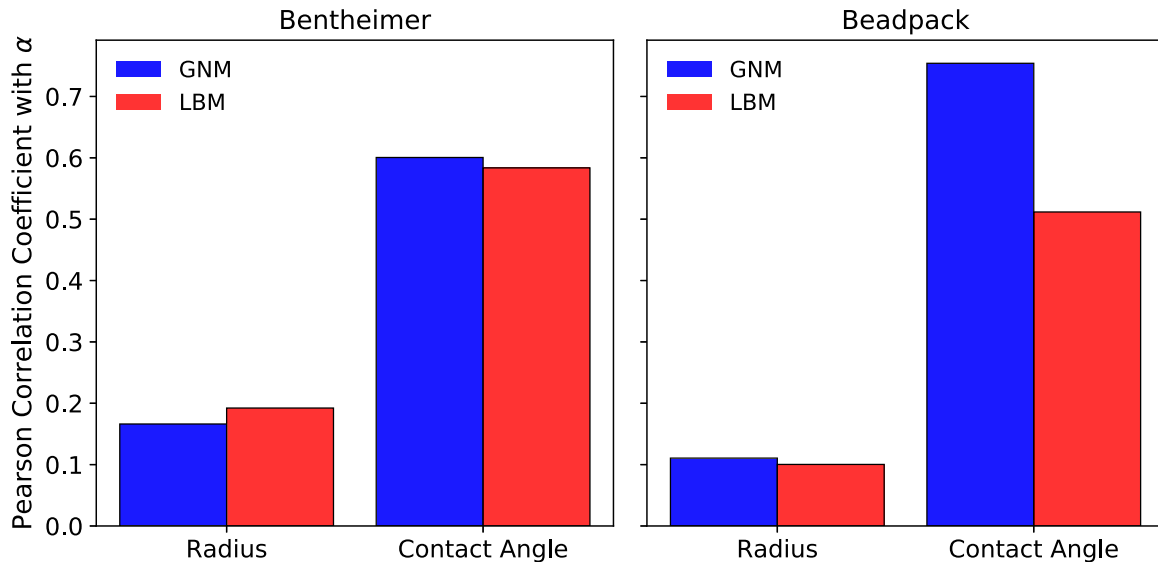
FIG. 11. A comparison of the Pearson correlation [Eq. (3)] of pore occupancy (α) with radius and contact angle, for both samples, for the mixed-wet simulations. GNM predictions are shown in blue while LBM predictions are in red.

like manner, while wetting layers are rarely pinned and can easily swell to allow an increase in wetting saturation before a change in occupancy occurs. The GNM can reproduce this behavior, while the LBM is limited to piston-like displacement and cooperative pore-filling of regions that are directly connected to the inlet, and all saturation changes occur due to the complete filling of regions in the pore-space. In addition, oil is preferentially retained in the largest regions of the pore-space (Fig. 8), where discrepancies have the most significant contribution to volume-weighted absolute differences, further exacerbating the mismatch. In the mixed-wet case, ordinary percolation still occurs in the water-wet regions, but is overall less prevalent than in the water-wet case; displacement in the oil-wet regions is controlled by simpler, invasion percolation-like behavior. Furthermore, in the oil-wet regions of the GNM, wetting layers become pinned and cannot accommodate wetting-phase saturation increases as easily as in water-wet regions: changes in saturation are more likely due to a change in occupancy, as in the LBM, contributing to lower mismatch than in the water-wet cases. As the pore-by-pore contact angle is assigned based on the oil saturation after primary drainage, and oil saturation is positively correlated with radius (Fig. 8), it follows that the more predictable oil-wet regions account for the largest pores in the system and thus reduce the volume-weighted discrepancies shown in Fig. 10 further. This is explored in more depth in Fig. 11, discussed later. In the oil-wet scenario, invasion percolation dominates, with filling purely in decreasing order of size, and the two models exhibit lower mismatch because of this simpler behavior, particularly in occupancy where the smallest pores are likely to remain occupied but have less contribution to volume-weighted differences. The exception to the observation of decreasing mismatch with wettability is the relative saturation mismatch for the oil-wet Bentheimer, which shows larger discrepancy due to the presence of oil-layers remaining stable in the angular pore-space, whereas the less angular pore-space of the beadpack is not conducive to their formation.

Second, the relative absolute discrepancies in predictions for the Bentheimer sample are generally larger than for the beadpack. This is an interesting finding: Raeini *et al.*'s [54] comparisons of the GNM to experiments, and indeed uncertainty quantification between repeat experiments, showed higher mismatch in a Ketton sample (comparable in resolvable pore morphology to a beadpack) over a Bentheimer sandstone. Possible explanations for the greater disagreement in Bentheimer shown here could be that: (i) there is a larger difference in S_{wi} between the GNM and LBM for Bentheimer; (ii) the effective resolution is greater in the beadpack, and (iii) Bentheimer has a more angular pore-space. Initial water saturation has been shown to be a sensitive parameter in pore-by-pore predictions [54] and so it is expected that a larger difference in initial condition could result in larger differences toward the end of waterflooding; however, the effect of this is mitigated to a certain extent through normalizing by Eqs. (6) and (7)—Fig. 10 shows similar discrepancy for both samples at the end of drainage but large differences in discrepancy after waterflooding. Figure 1, however, shows that the pores present in the beadpack are larger than in Bentheimer, and hence are better resolved for both the GNM and LBM, potentially reducing the disagreement for the beadpack. The one exception to this is the water-wet case, discussed previously, where the larger pores of the beadpack cause mismatches in the occupancy of the largest pores to yield greater volume-weighted absolute differences. Last, the narrower and more angular pore-space of Bentheimer is also more conducive to the formation and preservation of layer flow, which as discussed earlier is not a feature present in LBM at this resolution. Although small, layers can lead to large pore-by-pore differences—one can envisage the effect of a critical throat, for example, which experiences snap-off and blocks a flow path. Even without considering trapping phenomena, the presence of layers changes the saturation and entry pressures for any given element. The lower capillary pressures exhibited by the LBM in the water-wet cases of Fig. 5 are partly attributable to this. The above factors all impact the predictions

of the displacement sequence throughout the waterflooding, and the relative importance of each cause requires future investigation.

Returning to the discussion of occupancy in mixed-wet states, previous studies have demonstrated that displacement is not purely governed by size in mixed-wet media—wettability is also a determining factor [50,68]. The details of this, however, have not been fully explored. Figure 11 compares the Pearson correlation coefficient [Eq. (3)] of pore occupancy with radius and contact angle for the mixed-wet state, when the mean difference in pore-saturation is zero (Fig. 4), for both samples. It is clear that contact angle, rather than geometry, is the main control over whether a pore has remained occupied, as observed experimentally [60,68]. The GNM predicts a larger correlation with contact angle in both samples, explained by Fig. 6—ordinary percolation in the GNM can select water-wet regions, whereas the LBM cannot. Interestingly, the GNM predicts a stronger correlation of occupancy with contact angle in the beadpack over Bentheimer. This could be a feature of the topology of the two systems—with a higher coordination number, an invaded element in the beadpack could have more freedom to select surrounding water-wet pores to invade compared to Bentheimer. The extent to which topology controls the degree of occupancy correlation with local contact angle will be pursued in future studies.

Finally, it is noted that, for Bentheimer sandstone, the pore-by-pore mismatch between models is greater than the mismatch between repeat experiments [54]. At first, this is an unexpected finding as the uncertainty in pore-by-pore wettability is removed from this study but is not reflected in the difference between models. However, semianalytic approximations to flow and geometric approximations within the GNM are still present, and the initial water saturation at the end of drainage is also different between studies. Further, while wettability has been accounted for, discretization limitations within the LBM prohibit the implementation of layer flow using commonly deployed hardware. Whether wetting layers or oil layers, these features are routinely incorporated into network modeling and their impact has been experimentally proven. It is likely that their absence in this work accounts for a significant portion of the difference shown here.

IV. CONCLUSIONS AND FUTURE WORK

In this study, a workflow to compare pore-scale models of two-phase flow at both macroscopic and local scales is developed, implementing a spatial match in wettability. The method allows detailed insights into the pore-scale displacement and can be used to identify strengths and shortcomings

in predictive capability. The method was applied to analyze predictions obtained with a color-gradient lattice-Boltzmann model and the generalized network model for two-phase flow in two samples, a synthetic beadpack and a micro-CT imaged Bentheimer sandstone, for four displacements: primary drainage and waterflooding under water-wet, mixed-wet, and oil-wet conditions.

The comparison of macroscopic capillary pressure revealed good agreement between the two models, and experiments, at intermediate saturations but showed large discrepancies at the end-points. With a resolution of 10 grid blocks per average throat, the LBM is unable to reach low initial water saturations due to the absence of layers, which manifests as further differences during waterflooding in altered-wetting states. Critically, at the resolutions typically implemented in research settings, the LBM does not capture displacement by ordinary percolation in a mixed-wet state. The absence of layers further impacts the residual oil-saturations, with the LBM predicting higher values than expected.

In contrast, the GNM was able to capture the effect of layer flow and its impacts since, while the geometry of the pore space is simplified, layer flow can be described with infinite resolution. The GNM exhibits spontaneous imbibition in mixed-wet displacement, and lower residuals in altered wetting states. The GNM predictions also agree more closely with experimental waterflood measurements. At a pore-by-pore level, absolute differences larger than between repeat experiments are observed, further emphasizing that care must be taken when selecting pore-scale models. Overall, the comparison shows that network modeling is an attractive option for cost and time-effective prediction of two-phase flow.

Future work is to extend the comparison of the GNM to experimental observations of mixed-wet states in a wider variety of porous media, and to incorporate the effects of unresolved microporosity. Furthermore, the role of direct simulation in informing and calibrating network models at the pore scale should be explored, rather than expecting direct models to provide reliable estimates of macroscopic properties at the REV scale using standard computer resources for complex wetting states.

[1] A. Alhosani, A. Scanziani, Q. Lin, Z. Pan, B. Bijeljic, and M. J. Blunt, In situ pore-scale analysis of oil recovery during three-phase near-miscible CO_2 injection in a water-wet carbonate rock, Adv. Water Resour. **134**, 103432 (2019).

[2] J. Bear and A. H.-D. Cheng, *Modeling Groundwater Flow and Contaminant Transport* (Springer Science & Business Media, Cham, 2010), Vol. 23.

[3] M. E. Boot-Handford, J. C. Abanades, E. J. Anthony, M. J. Blunt, S. Brandani, N. Mac Dowell, J. R. Fernández, M. C.

Ferrari, R. Gross, J. P. Hallett, R. S. Haszeldine, P. Heptonstall, A. Lyngfelt, Z. Makuch, E. Mangano, R. T. Porter, M. Pourkashanian, G. T. Rochelle, N. Shah, J. G. Yao *et al.*, Carbon capture and storage update, Energy Environ. Sci. **7**, 130 (2014).

[4] P. C. Okonkwo and C. Otor, A review of gas diffusion layer properties and water management in proton exchange membrane fuel cell system, Int. J. Energy Res. **45**, 3780 (2021).

[5] R. Mittal, R. Ni, and J. H. Seo, The flow physics of COVID-19, J. Fluid Mech. **894**, F2 (2020).

[6] D. Wildenschild and A. P. Sheppard, X-ray imaging and analysis techniques for quantifying pore-scale structure and processes in subsurface porous medium systems, Adv. Water Resour. **51**, 217 (2013).

[7] M. J. Blunt, B. Bijeljic, H. Dong, O. Gharbi, S. Iglauer, P. Mostaghimi, A. Paluszny, and C. Pentland, Pore-scale imaging and modeling, Adv. Water Resour. **51**, 197 (2013).

[8] S. Berg, H. Ott, S. A. Klapp, A. Schwing, R. Neiteler, N. Brussee, A. Makurat, L. Leu, F. Enzmann, J. O. Schwarz, M. Kersten, S. Irvine, and M. Stampanoni, Real-time 3D imaging of Haines jumps in porous media flow, Proc. Natl. Acad. Sci. USA **110**, 3755 (2013).

[9] C. Knutson, A. Valocchi, and C. Werth, Comparison of continuum and pore-scale models of nutrient biodegradation under transverse mixing conditions, Adv. Water Resour. **30**, 1421 (2007).

[10] C. Varloteaux, M. T. Vu, S. Békri, and P. M. Adler, Reactive transport in porous media: Pore-network model approach compared to pore-scale model, Phys. Rev. E **87**, 023010 (2013).

[11] M. A. Sadeghi, M. Agnaou, J. Barralet, and J. Gostick, Dispersion modeling in pore networks: A comparison of common pore-scale models and alternative approaches, J. Contam. Hydrol. **228**, 103578 (2020).

[12] H.-J. Vogel, J. Tölke, V. P. Schulz, M. Krafczyk, and K. Roth, Comparison of a lattice-Boltzmann model, a full-morphology model, and a pore network model for determining capillary pressure-saturation relationships, Vadose Zone J. **4**, 380 (2005).

[13] B. Ahrenholz, J. Tölke, P. Lehmann, A. Peters, A. Kaestner, M. Krafczyk, and W. Durner, Prediction of capillary hysteresis in a porous material using lattice-Boltzmann methods and comparison to experimental data and a morphological pore network model, Adv. Water Resour. **31**, 1151 (2008).

[14] A. H. Kohanpur, M. Rahromostaqim, A. J. Valocchi, and M. Sahimi, Two-phase flow of CO_2-brine in a heterogeneous sandstone: Characterization of the rock and comparison of the lattice-Boltzmann, pore-network, and direct numerical simulation methods, Adv. Water Resour. **135**, 103469 (2020).

[15] B. Zhao, C. W. MacMinn, B. K. Primkulov, Y. Chen, A. J. Valocchi, J. Zhao, Q. Kang, K. Bruning, J. E. McClure, C. T. Miller, A. Fakhari, D. Bolster, T. Hiller, M. Brinkmann, L. Cueto-Felgueroso, D. A. Cogswell, R. Verma, M. Prodanović, J. Maes, S. Geiger *et al.*, Comprehensive comparison of pore-scale models for multiphase flow in porous media, Proc. Natl. Acad. Sci. USA **116**, 13799 (2019).

[16] B. Zhao, C. W. MacMinn, and R. Juanes, Wettability control on multiphase flow in patterned microfluidics, Proc. Natl. Acad. Sci. USA **113**, 10251 (2016).

[17] S. S. Datta, T. S. Ramakrishnan, and D. A. Weitz, Mobilization of a trapped nonwetting fluid from a three-dimensional porous medium, Phys. Fluids **26**, 022002 (2014).

[18] M. J. Blunt, *Multiphase Flow in Permeable Media: A Pore-Scale Perspective* (Cambridge University Press, Cambridge, UK, 2017).

[19] J. Schmatz, J. L. Urai, S. Berg, and H. Ott, Nanoscale imaging of pore-scale fluid-fluid-solid contacts in sandstone, Geophys. Res. Lett. **42**, 2189 (2015).

[20] H. Huang, P. Meakin, and M. Liu, Computer simulation of two-phase immiscible fluid motion in unsaturated complex fractures using a volume of fluid method, Water Resour. Res. **41**, W12413 (2005).

[21] A. Q. Raeini, M. J. Blunt, and B. Bijeljic, Modeling two-phase flow in porous media at the pore scale using the volume-of-fluid method, J. Comput. Phys. **231**, 5653 (2012).

[22] C. Pan, M. Hilpert, and C. T. Miller, Lattice-Boltzmann simulation of two-phase flow in porous media, Water Resour. Res. **40**, W01501 (2004).

[23] M. L. Porter, M. G. Schaap, and D. Wildenschild, Lattice-Boltzmann simulations of the capillary pressure–saturation–interfacial area relationship for porous media, Adv. Water Resour. **32**, 1632 (2009).

[24] T. Akai, M. J. Blunt, and B. Bijeljic, Pore-scale numerical simulation of low salinity water flooding using the lattice Boltzmann method, J. Colloid Interface Sci. **566**, 444 (2020).

[25] A. M. Tartakovsky and P. Meakin, Pore scale modeling of immiscible and miscible fluid flows using smoothed particle hydrodynamics, Adv. Water Resour. **29**, 1464 (2006).

[26] A. Q. Raeini, M. J. Blunt, and B. Bijeljic, Direct simulations of two-phase flow on micro-CT images of porous media and upscaling of pore-scale forces, Adv. Water Resour. **74**, 116 (2014).

[27] J. E. McClure, J. F. Prins, and C. T. Miller, A novel heterogeneous algorithm to simulate multiphase flow in porous media on multicore CPU-GPU systems, Comput. Phys. Commun. **185**, 1865 (2014).

[28] S. An, H. Yu, and J. Yao, GPU-accelerated volumetric lattice Boltzmann method for porous media flow, J. Petrol. Sci. Eng. **156**, 546 (2017).

[29] I. Fatt, The network model of porous media, Trans AIME **207**, 144 (1956).

[30] P. H. Valvatne and M. J. Blunt, Predictive porescale modeling of two-phase flow in mixed wet media, Water Resour. Res. **40**, W07406 (2004).

[31] I. Bondino, G. Hamon, W. Kallel, and D. Kac, Relative permeabilities from simulation in 3D rock models and equivalent pore networks: Critical review and way forward, Petrophysics **54**, 538 (2013).

[32] A. Q. Raeini, B. Bijeljic, and M. J. Blunt, Generalized network modeling: Network extraction as a coarse-scale discretization of the void space of porous media, Phys. Rev. E **96**, 013312 (2017).

[33] A. Q. Raeini, B. Bijeljic, and M. J. Blunt, Generalized network modeling of capillary-dominated two-phase flow, Phys. Rev. E **97**, 023308 (2018).

[34] H. Dong and M. J. Blunt, Pore-network extraction from micro-computerized-tomography images, Phys. Rev. E **80**, 036307 (2009).

[35] L. M. Giudici, A. Q. Raeini, M. J. Blunt, and B. Bijeljic, Representation of fully three-dimensional interfacial curvature in pore-network models, Water Resour. Res. (2023) (to be published).

[36] T. Akai, Q. Lin, B. Bijeljic, and M. J. Blunt, Using energy balance to determine pore-scale wettability, J. Colloid Interface Sci. **576**, 486 (2020).

[37] T. Akai, B. Bijeljic, and M. J. Blunt, Wetting boundary condition for the color-gradient lattice Boltzmann method: Validation with analytical and experimental data, Adv. Water Resour. **116**, 56 (2018).

[38] T. Ramstad, P. E. Øren, and S. Bakke, Simulation of two-phase flow in reservoir rocks using a lattice Boltzmann method, SPE J. **15**, 917 (2010).

[39] P. Mostaghimi, M. J. Blunt, and B. Bijeljic, Computations of absolute permeability on micro-CT images, Math. Geosci. **45**, 103 (2013).

[40] J. Zhao, F. Qin, D. Derome, and J. Carmeliet, Simulation of quasistatic drainage displacement in porous media on pore-scale: Coupling lattice Boltzmann method and pore network model, J. Hydrol. **588**, 125080 (2020).

[41] G. Singh and N. Tiwari, Thin film dynamics using lattice Boltzmann method: Role of aspect ratio and surface wettability gradient, Phys. Fluids **34**, 072104 (2022).

[42] H. Huang and X.-y. Lu, Relative permeabilities and coupling effects in steady-state gas-liquid flow in porous media: A lattice Boltzmann study, Phys. Fluids **21**, 092104 (2009).

[43] Y. Liu, S. Zou, Y. He, S. Sun, Y. Ju, Q. Meng, and J. Cai, Influence of fractal surface roughness on multiphase flow behavior: Lattice Boltzmann simulation, Int. J. Multiphase Flow **134**, 103497 (2021).

[44] A. G. Yiotis, J. Psihogios, M. E. Kainourgiakis, A. Papaioannou, and A. K. Stubos, A lattice Boltzmann study of viscous coupling effects in immiscible two-phase flow in porous media, Colloids Surf. A **300**, 35 (2007).

[45] A. D. Angelopoulos, V. N. Paunov, V. N. Burganos, and A. C. Payatakes, Lattice Boltzmann simulation of nonideal vapor-liquid flow in porous media, Phys. Rev. E **57**, 3237 (1998).

[46] S. Zitz, A. Scagliarini, S. Maddu, A. A. Darhuber, and J. Harting, Lattice Boltzmann method for thin-liquid-film hydrodynamics, Phys. Rev. E **100**, 033313 (2019).

[47] S. Leclaire, A. Parmigiani, O. Malaspinas, B. Chopard, and J. Latt, Generalized three-dimensional lattice Boltzmann color-gradient method for immiscible two-phase pore-scale imbibition and drainage in porous media, Phys. Rev. E **95**, 033306 (2017).

[48] E. S. Boek, I. Zacharoudiou, F. Gray, S. M. Shah, J. P. Crawshaw, and J. Yang, Multiphase-flow and reactive-transport validation studies at the pore scale by use of lattice Boltzmann computer simulations, SPE J. **22**, 940 (2017).

[49] Q. Lin, B. Bijeljic, R. Pini, M. J. Blunt, and S. Krevor, Imaging and measurement of pore-scale interfacial curvature to determine capillary pressure simultaneously with relative permeability, Water Resour. Res. **54**, 7046 (2018).

[50] Q. Lin, B. Bijeljic, S. Berg, R. Pini, M. J. Blunt, and S. Krevor, Minimal surfaces in porous media: Pore-scale imaging of multiphase flow in an altered-wettability Bentheimer sandstone, Phys. Rev. E **99**, 063105 (2019).

[51] S. Foroughi, B. Bijeljic, Q. Lin, A. Q. Raeini, and M. J. Blunt, Pore-by-pore modeling, analysis, and prediction of two-phase flow in mixed-wet rocks, Phys. Rev. E **102**, 023302 (2020).

[52] M. Andrew, B. Bijeljic, and M. J. Blunt, Porebypore capillary pressure measurements using Xray microtomography at reservoir conditions: Curvature, snapoff, and remobilization of residual CO_2, Water Resour. Res. **50**, 8760 (2014).

[53] S. Krevor, M. J. Blunt, S. M. Benson, C. H. Pentland, C. Reynolds, A. Al-Menhali, and B. Niu, Capillary trapping for geologic carbon dioxide storage—From pore scale physics to field scale implications, Int. J. Greenhouse Gas Control **40**, 221 (2015).

[54] A. Q. Raeini, J. Yang, I. Bondino, T. Bultreys, M. J. Blunt, and B. Bijeljic, Validating the generalized pore network model using micro-CT images of two-phase flow, Transp. Porous Media **130**, 405 (2019).

[55] B. Raeesi, N. R. Morrow, and G. Mason, Capillary pressure hysteresis behavior of three sandstones measured with a multistep outflow-inflow apparatus, Vadose Zone J. **13**, 1 (2014).

[56] N. R. Morrow, Irreducible wetting-phase saturations in porous media, Chem. Eng. Sci. **25**, 1799 (1970).

[57] F. A. Dullien, C. Zarcone, I. F. Macdonald, A. Collins, and R. D. Bochard, The effects of surface roughness on the capillary pressure curves and the heights of capillary rise in glass bead packs, J. Colloid Interface Sci. **127**, 362 (1989).

[58] R. Lenormand, C. Zarcone, and A. Sarr, Mechanisms of the displacement of one fluid by another in a network of capillary ducts, J. Fluid Mech. **135**, 337 (1983).

[59] M. Andrew, H. Menke, M. J. Blunt, and B. Bijeljic, The imaging of dynamic multiphase fluid flow using synchrotron-based x-ray microtomography at reservoir conditions, Transp. Porous Media **110**, 1 (2015).

[60] Y. Gao, A. Q. Raeini, A. M. Selem, I. Bondino, M. J. Blunt, and B. Bijeljic, Pore-scale imaging with measurement of relative permeability and capillary pressure on the same reservoir sandstone sample under water-wet and mixed-wet conditions, Adv. Water Resour. **146**, 103786 (2020).

[61] K. Singh, B. Bijeljic, and M. J. Blunt, Imaging of oil layers, curvature and contact angle in a mixedwet and a waterwet carbonate rock, Water Resour. Res. **52**, 1716 (2016).

[62] A. R. Kovscek, H. Wong, and C. J. Radke, A porelevel scenario for the development of mixed wettability in oil reservoirs, AIChE J. **39**, 1072 (1993).

[63] R. A. Salathiel, Oil recovery by surface film drainage in mixed-wettability rocks, J. Pet. Technol. **25**, 1216 (1973).

[64] A. L. Herring, A. Sheppard, L. Andersson, and D. Wildenschild, Impact of wettability alteration on 3D nonwetting phase trapping and transport, Int. J. Greenhouse Gas Control **46**, 175 (2016).

[65] N. Alyafei and M. J. Blunt, The effect of wettability on capillary trapping in carbonates, Adv. Water Resour. **90**, 36 (2016).

[66] J. Roof, Snap-off of oil droplets in water-wet pores, Soc. Pet. Eng. J. **10**, 85 (1970).

[67] A. Scanziani, K. Singh, T. Bultreys, B. Bijeljic, and M. J. Blunt, In situ characterization of immiscible three-phase flow at the pore scale for a water-wet carbonate rock, Adv. Water Resour. **121**, 446 (2018).

[68] A. Scanziani, Q. Lin, and M. J. Blunt, Dynamics of fluid displacement in mixed-wet porous media, Proc. R. Soc. A **476**, 20200040 (2020).

[69] M. Rücker, W. B. Bartels, T. Bultreys, M. Boone, K. Singh, G. Garfi, A. Scanziani, C. Spurin, S. Yesufu-Rufai, S. Krevor, M. J. Blunt, O. Wilson, H. Mahani, V. Cnudde, P. F. Luckham, A. Georgiadis, and S. Berg, Workflow for upscaling wettability from the nanoscale to core scale, Petrophysics **61**, 189 (2020).

[70] A. Alhosani, A. Scanziani, Q. Lin, S. Foroughi, A. M. Alhammadi, M. J. Blunt, and B. Bijeljic, Dynamics of water injection in an oil-wet reservoir rock at subsurface conditions: Invasion patterns and pore-filling events, Phys. Rev. E **102**, 023110 (2020).

[71] M. Andrew, B. Bijeljic, and M. J. Blunt, Pore-scale contact angle measurements at reservoir conditions using x-ray micro-tomography, Adv. Water Resour. **68**, 24 (2014).

[72] Y. Gao, Q. Lin, B. Bijeljic, and M. J. Blunt, X-ray microtomography of intermittency in multiphase flow at steady state using a differential imaging method, Water Resour. Res. **53**, 10274 (2017).

[73] K. Singh, H. Menke, M. Andrew, Q. Lin, C. Rau, M. J. Blunt, and B. Bijeljic, Dynamics of snap-off and pore-filling events during two-phase fluid flow in permeable media, Sci. Rep. **7**, 1 (2017).